



**HAL**  
open science

## Metal and acid sites instantaneously prepared over Ni/SAPO-11 bifunctional catalyst

Yuchao Lyu, Zhumo Yu, Ye Yang, Yuxiang Liu, Xinxin Zhao, Xinmei Liu,  
Svetlana Mintova, Zifeng Yan, Guofeng Zhao

► **To cite this version:**

Yuchao Lyu, Zhumo Yu, Ye Yang, Yuxiang Liu, Xinxin Zhao, et al.. Metal and acid sites instantaneously prepared over Ni/SAPO-11 bifunctional catalyst. *Journal of Catalysis*, 2019, 374, pp.208-216. 10.1016/j.jcat.2019.04.031 . hal-02409876

**HAL Id: hal-02409876**

**<https://hal.science/hal-02409876v1>**

Submitted on 27 Nov 2020

**HAL** is a multi-disciplinary open access archive for the deposit and dissemination of scientific research documents, whether they are published or not. The documents may come from teaching and research institutions in France or abroad, or from public or private research centers.

L'archive ouverte pluridisciplinaire **HAL**, est destinée au dépôt et à la diffusion de documents scientifiques de niveau recherche, publiés ou non, émanant des établissements d'enseignement et de recherche français ou étrangers, des laboratoires publics ou privés.

# **Metal and acid sites instantaneously prepared over Ni/SAPO-11 bifunctional catalyst**

Yuchao Lyu<sup>a, b</sup>, Zhumo Yu<sup>a</sup>, Ye Yang<sup>a</sup>, Yuxiang Liu<sup>a</sup>, Xinxin Zhao<sup>a</sup>, Xinmei Liu<sup>a,\*</sup>, Svetlana Mintova<sup>a,c</sup>, Zifeng Yan<sup>a</sup>, Guofeng Zhao<sup>d</sup>

<sup>a</sup> *State Key Laboratory of Heavy Oil Processing, China University of Petroleum, Qingdao 266555, China*

<sup>b</sup> *EMS Energy Institute, The Pennsylvania State University, University Park, PA, 16802, USA*

<sup>c</sup> *Laboratoire Catalyse & Spectrochimie, ENSICAEN, Université de Caen, 14000, Caen, France*

<sup>d</sup> *Shanghai Key Laboratory of Green Chemistry and Chemical Processes, School of Chemistry and Molecular Engineering, East China Normal University, Shanghai 200062, China*

**Keywords:** Nickel; SAPO-11; Synthesis; Bifunctional catalyst; Hydroisomerization

---

\*Corresponding author at State Key Laboratory of Heavy Oil Processing, China University of Petroleum, Qingdao 266555, China  
E-mail address: [lxmei@upc.edu.cn](mailto:lxmei@upc.edu.cn) (X.Liu).

## Abstract

The Ni/SAPO-11 bifunctional catalyst for hydroisomerization of n-hexane was prepared via a novel synthesis method. It involved grinding of nickel source with amorphous precursors used for SAPO-11 followed by crystallization at 473 K for 24 h, thus avoiding the use of extra solvents in the synthesis. The highly dispersed nickel species and acid sites in the Ni/SAPO-11 bifunctional catalyst were instantaneously formed. The Ni/SAPO-11 catalyst contains framework nickel, nickel monoxide (NiO) and nickel aluminate spinel. The nickel monoxide with a size of 2-4 nm provides (de)hydrogenation function after reduction, while the framework nickel supplies more acid sites leading to an enhanced isomerization activity. The Ni/SAPO-11 catalyst shows a great synergetic effect between the metallic nickel and acid sites with a high metal-to-acid sites ratio ( $C_{Ni}/C_A$ ) and close proximity. A single metallic nickel site is able to balance ca. 5 acid sites ( $C_{Ni}/C_A \approx 0.19$ ) over the Ni/SAPO-11 catalyst in n-hexane hydroisomerization. The high dispersion of nickel over the catalyst provides relatively excessive metal sites ( $C_{Ni}/C_A > 0.19$ ), leaving the rate limiting reaction to occur on the acid sites. The Ni/SAPO-11 catalyst exhibits comparable n-hexane conversion (71.2%) and iso-hexane yield (66.7%) to the classical Pt/SAPO-11 catalyst. With enhancing acidity, the Ni/SAPO-11 catalyst exhibits one of the highest iso-hexane yields reported in the n-hexane hydroisomerization, which render the new material as a promising candidate for the hydroisomerization catalysts.

## 1. Introduction

Hydroisomerization of light n-alkanes is an important catalytic process to obtain clean gasoline with high octane number [1-3]. Increasing proportion of the isomerized gasoline in the gasoline pool contributes to the products upgrading and environmental protection[2, 4, 5].The current catalysts used in the hydroisomerization process are bifunctional, namely containing acid sites for skeletal isomerization and metal sites for (de)hydrogenation[6, 7].Noble metals (platinum, palladium) are widely used in the bifunctional catalysts[2, 8-10], but suffer from limited availability and high costs. The widely used Pt-promoted chlorinated alumina catalysts cause serious corrosion problems and environmental pollution due to the need of continuous chlorine addition [11]. Therefore, the development of non-noble metal (nickel) based hydroisomerization catalysts is an appealing task. Several attempts have been made to prepare non-noble metal catalysts, and it has been shown that large metal particles are formed caused by a severe sintering which is unavoidable especially at high metal loading[12, 13]. This problem restricts the optimization of the existing non-noble catalysts. Therefore, it is vital to look for a novel strategy for preparation of the non-noble metals with reduced particle sizes for hydroisomerization catalysts.

In order to reduce the particle size of metal species in catalysts, strengthening of the interactions between the metal species and support to inhibit the metals aggregation is of critical importance[14, 15]. Using the impregnation method with solvents with weak polarities is an effective way to achieve this goal[16-19]. In the previous work[13], ethanol was used as solvent to support nickel on SAPO-11 and to produce Ni/SAPO-11 catalyst. The particle size of nickel monoxide (20 nm) was much smaller than that over the catalyst prepared with water as solvent (50 nm). Compared with the conventional impregnation

method, a stronger metal-support interaction can be obtained through equilibrium adsorption method. The metal species were deposited through adsorption and reaction with receptor sites developed on the support [20]. Goula et al. [21] prepared Ni/Al<sub>2</sub>O<sub>3</sub> by equilibrium adsorption method for the biogas dry reforming reaction. They found that a smaller metal particle size of 8 nm was obtained through this method compared with metal particles of 13 nm of the catalysts prepared by the impregnation method; the former catalyst showed enhanced catalytic performance. Controllable adsorption method could also be used to strengthen the metal-support interaction in Ni/Al<sub>2</sub>O<sub>3</sub> catalysts. Optimal adsorption conditions were identified using point of zero charge, pH precipitation and adsorption experiments [22]. The Ni/Al<sub>2</sub>O<sub>3</sub> catalyst prepared under such conditions presented a stronger metal-support interaction and higher metal dispersion than the catalyst prepared by impregnation. Many other trials including introduction of additives [23-25] or changing metal precursors [10, 26, 27] to inhibit the aggregation of metal species have been performed.

However, most of these methods lead to more complex synthesis procedures, violating the green synthesis of the catalyst. Besides, the main focus is on metal dispersion without paying due attention to acidity. Even more the acid sites on supports during the impregnation or adsorption of metal precursor are modified. This is not a favorable situation for bifunctional catalysts whose performance depends not only on the metal sites, but also on the acidity and metal-acid balance.

In the present work, direct synthesis method was used for instantaneous synthesis of highly-dispersed nickel species and acid sites over the Ni/SAPO-11 hydroisomerization catalyst. The synthesis method involved initial grinding of SAPO-11 precursors with nickel

source without extra solvents followed by crystallization. This method leads to significant reduction of waste and solvent use as well as the synthesis procedure is shortened significantly. It differs from the solvent-free method that requires pre-reaction of the raw materials and washing of intermediates with ethanol [28, 29]. The features of metal and acid sites over the Ni/SAPO-11 catalyst were investigated systematically. The catalytic performance was assessed by hydroisomerization of n-hexane, and active site for (de)hydrogenation reaction was disclosed. The metal-acid balance and reaction pathway were also discussed.

## 2. Experimental

### 2.1 Materials

Pseudo-boehmite (70.0 wt.%  $\text{Al}_2\text{O}_3$ ) was purchased from Yantai Henghui Petrochemical Co., Ltd. Phosphoric acid (85.0 wt.%  $\text{H}_3\text{PO}_4$ ) was purchased from XiRong Petrochemical Co., Ltd. Di-propylamine (DPA,  $\geq 99.0$  wt.%  $\text{C}_6\text{H}_{15}\text{N}$ ) and Nickel (II) nitrate hexahydrate ( $\text{Ni}(\text{NO}_3)_2 \cdot 6\text{H}_2\text{O}$ ) were purchased from Sinopharm Chemical Reagent Co., Ltd. Silica sol (30.0 wt.%  $\text{SiO}_2$ ) was purchased from Qingdao Haiyang Petrochemical Co., Ltd. All chemicals were used without purification.

### 2.2 Sample synthesis

Direct synthesis of Ni/SAPO-11(s) was carried out using a mixture with the following molar ratio: 1.0  $\text{P}_2\text{O}_5$ : 1.9 DPA: 0.4  $\text{SiO}_2$ : 0.19  $\text{Ni}(\text{NO}_3)_2 \cdot 6\text{H}_2\text{O}$ : 1.0  $\text{Al}_2\text{O}_3$ . In a typical run, 4.38 g of pseudo-boehmite, 6.92 g of  $\text{H}_3\text{PO}_4$ , 5.76 g DPA, 2.4 g of silica sol and 1.65 g of  $\text{Ni}(\text{NO}_3)_2 \cdot 6\text{H}_2\text{O}$  were mixed in a mortar. After grinding for 10 min, the mixture was transformed to an autoclave and heated at 473 K for 24 h. The solid product was washed with

deionized water, dried at 373 K for 12 h and calcined at 773 K in a muffle oven for 6 h. Varying the amount of nickel addition, catalysts with different nickel loading were prepared. When H-Beta zeolite was added into the initial synthesis gel of the Ni/SAPO-11(s), the final product was abbreviated as Ni/SAPO-11- $\beta$ (s). The mass ratio of H-Beta relative to the alumina source used for the SAPO-11 (pseudo-boehmite) was 0.1. As a reference, SAPO-11(s) without nickel was also prepared by the same procedure.

For comparison, two samples via incipient impregnation method abbreviated as Ni/SAPO-11(im) and Pt/SAPO-11(im) were prepared as follow: SAPO-11 was immersed in aqueous solutions of  $\text{Ni}(\text{NO}_3)_2 \cdot 6\text{H}_2\text{O}$  or  $\text{H}_2\text{PtCl}_6$ . After the impregnation, the material was dried at 383 K for 2 h and then calcined in air at 673 K for 4 h. The loading of nickel in the Ni/SAPO-11(im) sample was 4.0 wt.% that was the same as for the Ni/SAPO-11(s) sample; the loading of Pt was 0.3 wt.%. The SAPO-11 used for the impregnation was synthesized according to the procedure reported before [13].

### **2.3 Characterization**

X-ray diffraction (XRD) patterns of samples were collected with X' Pert PRO MPD diffractometer (PANalytical B.V. Netherlands) with Cu  $K\alpha$  radiation ( $\lambda = 0.15418$  nm) operated at 40 kV and 40 mA. Transmission electron microscopy (TEM) and elemental mapping of nickel were performed using a FEI Titan G2 80-200 TEM/STEM. The elemental mapping was obtained by energy dispersive X-ray spectroscopy using the super-X detector. X-ray photoelectron spectroscopy (XPS) was carried out using a PHI 500 spectrometer with Al  $K\alpha$  radiation. The binding energy was calibrated by measuring the C1s peak at 284.8 eV. Practical metal loading and chemical compositions of the samples were measured by X-ray

fluorescence (XRF, ZSX-100e using Rh and Au excitation tubes). X-ray absorption fine structure (XAFS) spectra were obtained at the 1W1B station in the BSRF (Beijing Synchrotron Radiation Facility, People's Republic of China) operated at 2.5 GeV with a maximum current of 250 mA. X-ray absorption spectroscopy (XAS) measurements at the Ni K-edge were performed in fluorescence mode using a Lytle detector. All samples were pelletized as disks of 13 mm diameter with 1 mm thickness using graphite powder as a binder. Temperature programmed reduction of hydrogen ( $H_2$ -TPR) and temperature programmed desorption of ammonia ( $NH_3$ -TPD) were carried out on a dynamic chemisorption analyzer (Micromeritics AutoChem 2920). The IR spectra of catalysts were recorded by a Nicolet-6700 FTIR spectrometer. The acidity of the catalysts was evaluated using pyridine as a probe molecule followed by FTIR. All samples were evacuated at 573 K for 3 h, followed by adsorption of pyridine at room temperature and desorption of pyridine in a vacuum at 423 K. Finally the spectra were recorded at room temperature.  $H_2$  chemisorption measurements were carried out on a Micromeritics AutoChem 2920; the accessible metal sites ( $C_{Ni}$ ) of the catalysts after reduction were studied. Prior to the chemisorption at ambient temperature, the samples were pretreated in hydrogen atmosphere at 823 K for 2 h and purged at this temperature in an argon flow for 2 h to avoid the presence of residual absorbed hydrogen. The ratio ( $C_{Ni}/C_A$ ) of metal sites ( $C_{Ni}$ ) relative to the acid sites ( $C_A$ ) was calculated according to the method disclosed before [30-32]. Ultraviolet-visible (UV-vis) diffuse reflectance spectra were recorded on a UV-2600 UV-vis spectrophotometer using  $BaSO_4$  as a reference. The turnover frequency (TOF) per acid site, labeled as  $TOF_{n-C6}$ , was calculated using the following equation:

$$\text{TOF}_{\text{n-C}_6} = \frac{\text{Rate of converted n-hexane (mol g}_{\text{cat}}^{-1} \text{ h}^{-1})}{\text{Number of acid sites (mol g}_{\text{cat}}^{-1})}$$

## 2.4 Catalytic Tests

The hydroisomerization of n-hexane (n-C<sub>6</sub>) was selected as a model reaction to assess the catalytic performance of the catalysts. The catalytic tests were carried out at a pressure of 2.0 MPa, a weight hourly space velocity (WHSV) of 1.0 h<sup>-1</sup>, and a H<sub>2</sub>/n-C<sub>6</sub> molar ratio of 4.0. Prior to the reaction, the catalyst was reduced in situ under a hydrogen flow at 823 K for 2 h and then cooled to reaction temperature. The reaction products were analyzed on-line by a gas chromatograph (Agilent 7820) equipped with a flame ionization detector. The n-hexane conversion might be increased due to the thermal behavior of the reaction at high temperature. The thermal reaction of the current feed was carried out at the highest temperature (653 K) in the present work. The n-hexane conversion was less than 1.0 %, indicating that in all cases investigated, thermal reaction did not bias the hydroisomerization results.

## 3. Results and discussion

### 3.1 Crystalline phases

Fig. 1 shows XRD patterns of the calcined Ni/SAPO-11(s), Ni/SAPO-11(im) and SAPO-11(s) samples. All the XRD patterns (Fig. 1 (a)) correspond to well-crystalline samples with the AEL type framework structure [33, 34]. The relative crystallinity of Ni/SAPO-11(s) increases compared with SAPO-11(s) and the growth of (002) crystal plane is enhanced mostly. Only a slight decrease in the peak width is observed for the Ni/SAPO-11(s) compared with the SAPO-11(s), which implies a small difference in grain size between the two samples. Thus, the increased crystallinity of the Ni/SAPO-11(s) might be due to the effective structure

directing effect of amine complex of nickel formed by nickel and di-propylamine in the synthesis gel of Ni/SAPO-11(s). Similar phenomenon was observed in the synthesis of aluminophosphates molecular sieves with nickel or cobalt complex of diethylenetriamine as a structure directing agent[35, 36]. In this case, part of nickel ultimately resided in tetrahedral sites in the framework of SAPO-11[36], which is confirmed by the slight shifting of the diffraction peak to a lower angle for the Ni/SAPO-11(s) (0.03 degree) compared with the SAPO-11(s) (Fig. 1(b)). The substitution of smaller tetrahedrally coordinated skeletal atoms (Al 0.51 Å or P 0.38 Å in crystal form) with heteroatoms of nickel that has a larger size (0.69 Å) as ions in crystalline environment, yields an increased lattice parameter value[37].

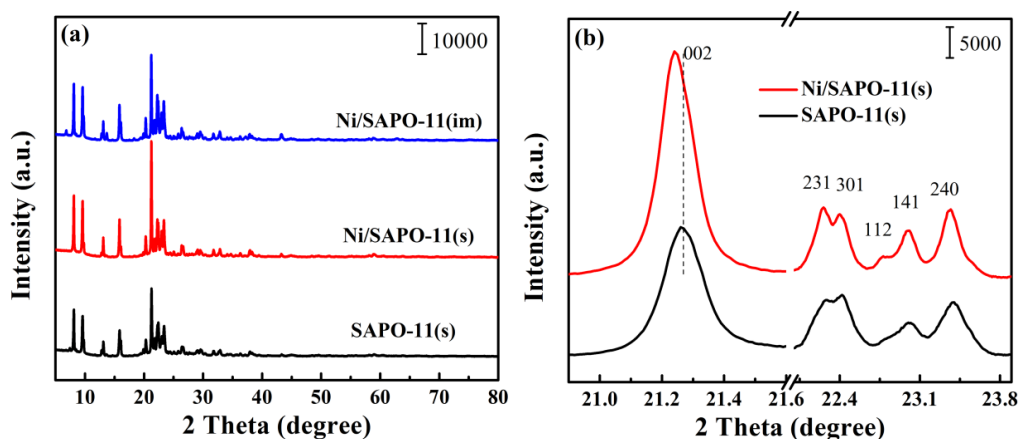


Fig. 1. XRD patterns of (a) as synthesized SAPO-11(s), calcined Ni/SAPO-11(s) and Ni/SAPO-11(im) in the range of 5-80° 2 Theta, and (b) SAPO-11(s) and calcined Ni/SAPO-11(s) in the range of 20.9-23.9° 2 Theta.

### 3.2 State of nickel Species

UV-vis diffuse reflectance spectra of the calcined catalysts are shown in Fig. 2; the spectrum of pure NiO is added as a reference. The UV-vis spectra of the Ni/SAPO-11(im) catalyst and the bulk NiO are very similar in bands positions, consisting of absorption bands at 280, 380, 420, 640 and 720 nm. This implies that the nickel in the Ni/SAPO-11(im) exists as

NiO[38]. For the Ni/SAPO-11(s), apart from the absorption bands assigned to the NiO, the new one at 257 nm is attributed to the electron transfer from  $O^{2-}$  (2p) to tetrahedral  $Ni^{2+}$  (3d) in framework of the SAPO-11[39-41]; the peak at 400 nm (Fig.2 (b)) is assigned to the octahedrally coordinated nickel species in nickel aluminate spinel[42, 43].

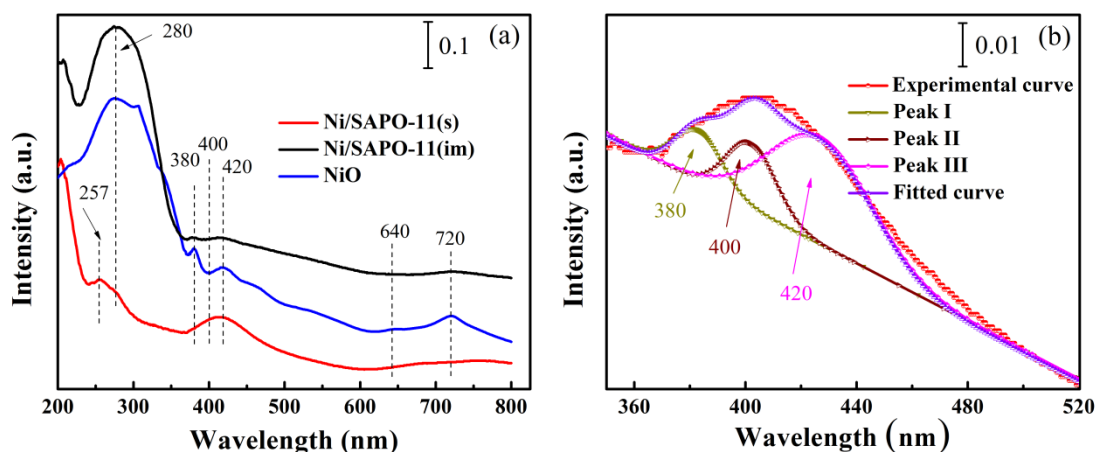


Fig. 2. UV-vis diffuse reflectance spectra of the calcined Ni/SAPO-11(s), Ni/SAPO-11(im) and bulk NiO samples (a) and peak simulation for the spectrum of sample Ni/SAPO-11(s) in the range of 350-520 nm (b)

XPS was also carried out to further elucidate the chemical environment and nature of nickel species in the Ni/SAPO-11(s) and Ni/SAPO-11(im) catalysts (Fig.3); the spectrum of bulk NiO is added as a reference. The Ni 2p region of the bulk NiO comprises four easily discernible features: the Ni 2p<sub>3/2</sub> main peak and its satellite at ~ 854.6 and ~ 861.2 eV, and the Ni 2p<sub>1/2</sub> main peak and its satellite at ~ 871.8 and ~ 879.1 eV. This result is consistent with the XPS spectrum of bulk NiO reported in literature[44]. However, the electronic structure is more complex. The two peaks at 853.8 and 855.4 eV in the Ni 2p<sub>3/2</sub> region after deconvolution can be explained in terms of a simplified model of final state effects in which photoemission is potentially accompanied by rearrangement of electrons in the valence band[45]. They shifted to higher binding energy (854.3 and 856.1 eV) for the Ni/SAPO-11(im) due to the interaction between NiO and the support. In contrast, for the

Ni/SAPO-11(s), the peak at 856.3 eV of Ni 2p<sub>3/2</sub>, together with the one at 873.6 eV of Ni 2p<sub>1/2</sub> indicate the existence of octahedral Ni<sup>2+</sup> in the NiO that strongly interacts with the SAPO-11[46, 47]. The peaks at 857.6 and 875.3 eV, which are in the range of Ni 2p<sub>3/2</sub> and Ni 2p<sub>1/2</sub>, respectively, are assigned to nickel aluminate spinel[48]. The small peaks at 859.0 (Ni 2p<sub>3/2</sub>) and 876.9 eV (Ni 2p<sub>1/2</sub>) can be assigned to tetrahedral Ni<sup>2+</sup> in the framework of SAPO-11 [46], which is also supported by the UV-vis results.

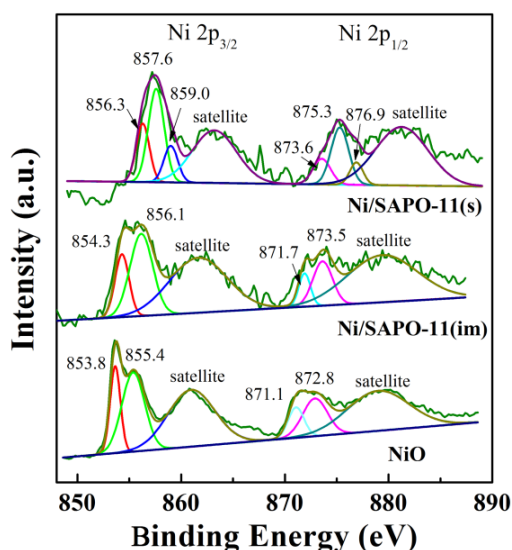


Fig. 3. XPS spectra of the Ni2p core level for calcined Ni/SAPO-11(s), Ni/SAPO-11(im) and bulk NiO samples recorded at room temperature

X-ray absorption near-edge structure (XANES) was carried out to provide further insights into the electronic structure of nickel in the Ni-SAPO-11(s) (Fig.4). Compared with the NiO reference, white line of the Ni/SAPO-11(s) shifts towards lower energy, probably due to the formation of tetrahedral Ni<sup>2+</sup> [49] in the SAPO-11 framework, consistent with the XRD, XPS and UV-vis results. The experimental and fitted EXAFS curves for the Ni/SAPO-11(s) catalyst is shown in Fig. S1, and Table S1 shows the average shell distances around the nickel atoms. The Ni-O distance of 2.09 Å and Ni-Ni distance of 2.96 Å are assigned to the

nickel in octahedral sites of NiO[50]. The average Ni-O distance of 1.97 Å is mainly assigned to the nickel aluminate spinel [51] that has predominant content in the nickel species as indicated by the strongest peak at 857.6 eV in XPS spectrum (Fig. 3) for the Ni/SAPO-11(s) catalyst. Meanwhile, Ni-P shell is also found by fitting confirming the incorporation of nickel into the framework of SAPO-11. In brief, three types of nickel species are identified in the calcined Ni/SAPO-11(s) catalyst: NiO, nickel aluminate spinel and framework nickel.

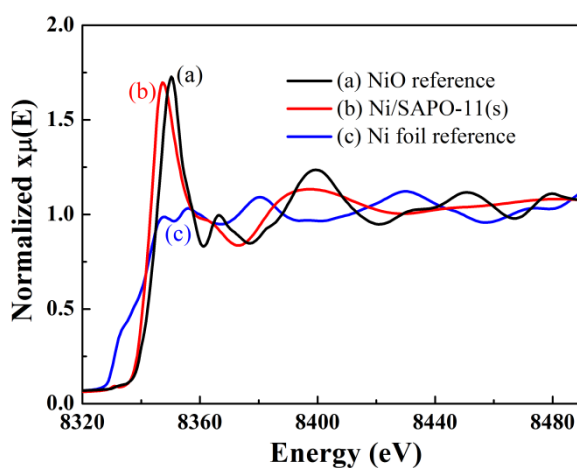


Fig. 4. XANES spectra at the Ni K-edge of (a) NiO reference, (b) Ni/SAPO-11(s) and (c) Ni foil reference.

Diffraction peaks of NiO are not observable for the Ni/SAPO-11(s) sample, but clearly the NiO peaks are seen in the Ni/SAPO-11(im) sample (see partly enlarged XRD patterns in Fig. S2). This indicates a higher dispersion of NiO in the Ni/SAPO-11(s) sample. The NiO spherical particles with a homogenous size (2-4 nm in diameter) and high dispersion in the Ni/SAPO-11(s) catalyst are observed (Fig. 5). Heavily agglomerated NiO particles with a size of 30-100 nm and sharp edge on the surface of the Ni/SAPO-11(im) catalyst are formed. Additionally, the elemental maps of nickel (Fig. 6(f)) also show that nickel species aggregated in some regions, showing an uneven distribution on the surface of the Ni/SAPO-11(im). The catalyst prepared by the direct method presents a uniform distribution of nickel (Fig. 6(c)).

The higher dispersion of nickel species could be ascribed to the spatial effect of the raw material used for the preparation of the SAPO-11 support. All the raw materials including the nickel source (nickel nitrate) were mixed with the precursor of SAPO-11 before the crystallization was performed in order to inhibit the contact between the nickel species.

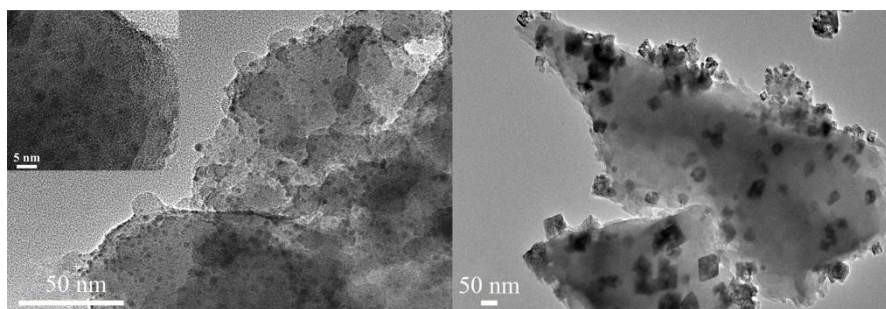


Fig. 5. TEM images of the calcined Ni/SAPO-11(s) (left) and Ni/SAPO-11(im) (right) catalysts

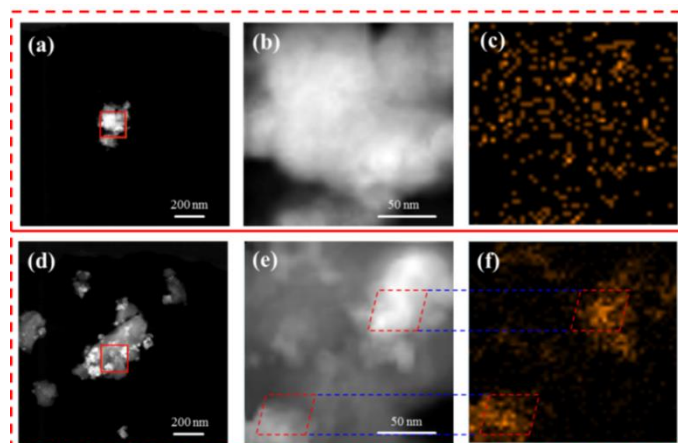


Fig.6. STEM images and the corresponding EDS elemental maps of nickel of calcined Ni/SAPO-11(s) (a, b and c) and Ni/SAPO-11(im) (d, e and f) catalysts

### 3.3 Reducibility

The H<sub>2</sub>-TPR profiles of samples Ni/SAPO-11(s), Ni/SAPO-11(im) and SAPO-11(s) are shown in Fig. 7. The Ni/SAPO-11(im) contains two peaks centering at ca. 643 and 715 K, which are assigned to the reduction of NiO with weak and strong interactions with SAPO-11, respectively[52]. Compared with Ni/SAPO-11(im), the Ni/SAPO-11(s) catalyst exhibits higher reduction temperature suggesting the stronger interaction between the nickel species

and the SAPO-11 support [53]. The maximum peak at 990 K is assigned to the reduction of nickel aluminate spinel[54]. The small shoulder at 1050 K is ascribed to the reduction of framework nickel species, supporting the incorporation of nickel into the framework of SAPO-11 as previously shown by UV-vis and XPS. Another distinct peak at ca. 823 K corresponds to the reduction of NiO strongly interacting with SAPO-11. The hydrogen consumption at ca. 1250 K is attributed to the reduction of  $\text{PO}_4^{3-}$  species in SAPO-11. Such high temperature is due to the high stability of P-O bond [55]. Notably, only NiO could be reduced during the reduction step according to the  $\text{H}_2$ -TPR profile of the Ni/SAPO-11(s) catalyst.

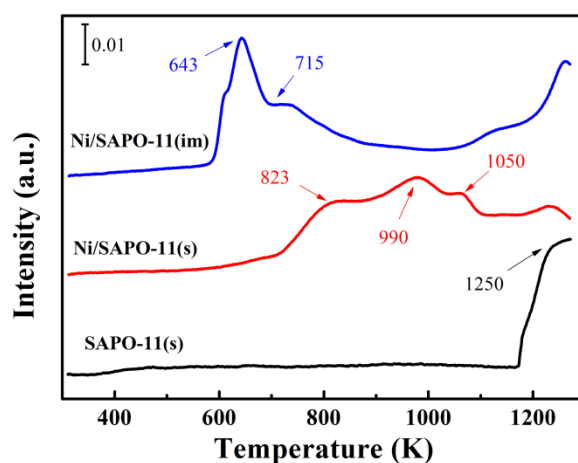


Fig. 7.  $\text{H}_2$ -TPR profiles of samples Ni/SAPO-11(s), Ni/SAPO-11(im) and SAPO-11(s)

### 3.4 Acidity

The FT-IR spectra of pyridine (Py-IR) adsorbed on reduced Ni/SAPO-11(s), Ni/SAPO-11(im) and SAPO-11(s) samples are depicted in Fig. 8. The IR bands at 1540 and 1450  $\text{cm}^{-1}$  are assigned to pyridine adsorbed on Brønsted and Lewis acid sites, respectively[56, 57]. Obviously, impregnated catalyst has less acid sites than the Ni/SAPO-11(s) catalyst. It should be noticed that the Ni/SAPO-11(s) has more Brønsted acid sites than the SAPO-11(s). The Ni/SAPO-11(s) and SAPO-11(s) exhibit similar compositions in terms of Si, P and Al

(Table S2). The increased Brønsted acid sites over the Ni/SAPO-11(s) catalyst are mainly contributed by the incorporation of divalent nickel ions into the SAPO-11 framework that introduces more negative charges, thus generating more Brønsted acid sites. The  $\text{Ni}^{2+}$  was most likely to substitute for  $\text{Al}^{3+}$  to form bridged NiP-OH structures in the Ni/SAPO-11(s) sample[58]. Similar phenomenon was observed in the metal-substituted  $\text{AlPO}_4$  molecular sieves[59]. The Brønsted acid sites from bridged MeP-OH ( $\text{Me}^{2+}$ ) in the MeAPO-11 sample are proposed to be strong[59] and this will be confirmed by the  $\text{NH}_3$ -TPD (see Fig. S3). The acid distribution of all catalysts is summarized in Table S3. The Ni/SAPO-11(s) catalyst shows more acid sites than the Ni/SAPO-11(im). The amount of weak acid sites for Ni/SAPO-11(s) and SAPO-11(s) is similar, while the Ni/SAPO-11(s) contains more medium and strong acid sites. The Py-IR spectra collected after desorption at different temperatures (Fig. S4) imply that the increased acid sites in the Ni/SAPO-11(s) are mainly composed of strong Brønsted acid sites.

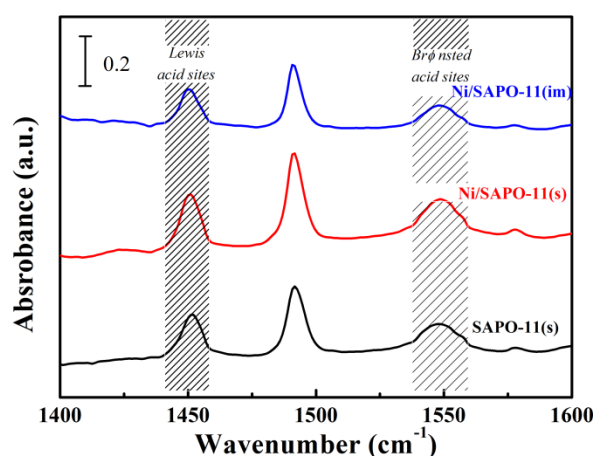


Fig.8. FT-IR spectra recorded under pyridine adsorption on SAPO-11(s), and reduced Ni/SAPO-11(s) and Ni/SAPO-11(im) catalysts

### 3.5 Metal sites for (de)hydrogenation reaction

Three types of nickel species in the Ni/SAPO-11(s) catalyst are identified as described

above. Given that only NiO could be reduced into metallic nickel during the reduction step and nickel aluminate spinel is inactive in n-hexane hydroisomerization, the reactions were carried out over SAPO-11(s), unreduced and reduced Ni/SAPO-11(s) samples at 593 K (Fig. 9). Compared with the SAPO-11(s), there is only a slight increase in the n-hexane conversion and iso-hexane (i-C<sub>6</sub>) yield over the unreduced catalyst. This increase is attributed to the contribution of weak (de)hydrogenation function of NiO and enhanced isomerization function by framework nickel species. In contrast, the n-C<sub>6</sub> conversion and i-C<sub>6</sub> yield over reduced Ni/SAPO-11(s) catalyst are much higher than that over the unreduced Ni/SAPO-11(s). This indicates that the active sites for (de)hydrogenation are provided predominantly by metallic nickel rather than by the framework nickel species.

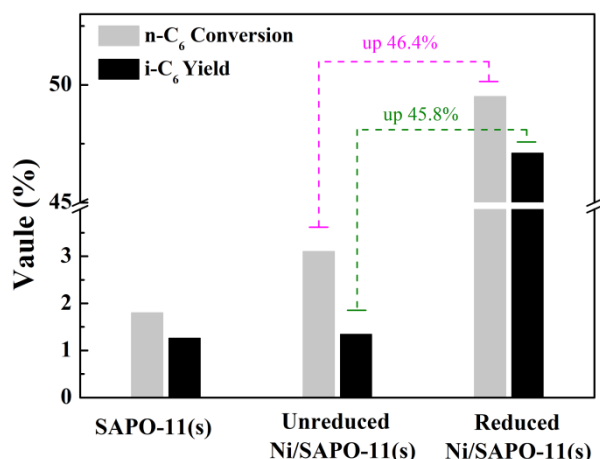


Fig. 9. Catalytic performance of SAPO-11(s), unreduced and reduced Ni/SAPO-11(s) catalysts

The nickel content and concentration of metallic nickel sites ( $C_{Ni}$ ) in the reduced catalysts are shown in Table 1. Obviously, the reduced Ni/SAPO-11(s) contains more metal sites on the surface in comparison to the reduced Ni/SAPO-11(im). This is attributed to the smaller Ni particles formed over the reduced Ni/SAPO-11(s) catalyst, which can be confirmed by the TEM images and Ni particle size distributions of the reduced Ni/SAPO-11(s) and Ni/SAPO-11(im) catalysts (Fig. S5). The Ni particles with a relative homogenous size (8-12

nm) are observed over the reduced Ni/SAPO-11(s) catalyst. In contrast, much bigger Ni particles (30-90 nm) are formed over the reduced Ni/SAPO-11(im) catalyst.

Table 1 Nickel content, nickel sites ( $C_{Ni}$ ), acid sites ( $C_A$ ) and the  $C_{Ni}/C_A$  ratio over the Ni/SAPO-11(s) and Ni/SAPO-11(im) catalysts

Sample	Ni content (wt %)	$C_{Ni}$ ( $\mu\text{mol/g}$ )	$C_A$ ( $\mu\text{mol/g}$ )	$C_{Ni}/C_A$
Ni/SAPO-11(s)	4.0	55.4	247.6	0.224
Ni/SAPO-11(im)	4.0	28.0	176.9	0.158

### 3.6 Catalytic test

The results from the catalytic tests of samples Ni/SAPO-11(s) and Ni/SAPO-11(im) are shown in Fig. 10; the Pt/SAPO-11(im) sample is used only for comparison (reference sample). The Ni/SAPO-11(s) shows much higher n-hexane conversion than the Ni/SAPO-11(im) in the whole reaction temperature range (Fig. 10 (a)). Compared with the reference Pt/SAPO-11(im), the Ni/SAPO-11(s) shows a slightly lower n-hexane conversion at temperature below 613 K. As the temperature increased, they exhibit almost the same n-hexane conversion, suggesting the high activity of the Ni/SAPO-11(s) catalyst.

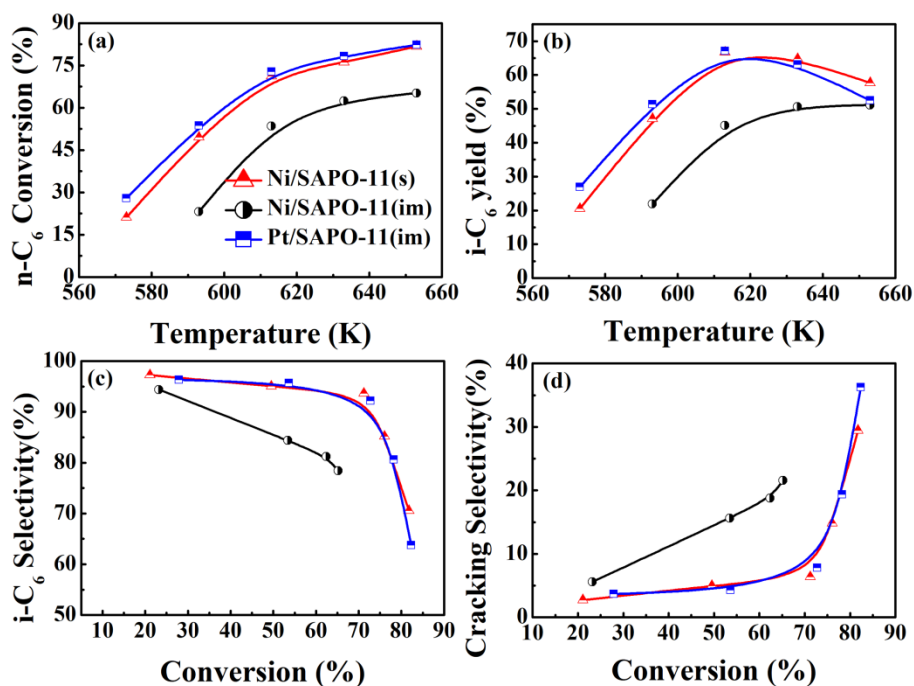


Fig. 10. Catalytic performance of samples Ni/SAPO-11(s), Ni/SAPO-11(im) and Pt/SAPO-11(im) (reference): n-C<sub>6</sub> conversion (a) and i-C<sub>6</sub> yield (b) versus temperature, selectivity to i-C<sub>6</sub> (c) and cracking products (< C<sub>6</sub>) (d) versus n-C<sub>6</sub> conversion

The iso-hexane selectivity decreases with n-hexane conversion over all the catalysts (Fig. 10 (c)), indicating the increased rate of side reaction at higher n-hexane conversion. The Ni/SAPO-11(s) and Pt/SAPO-11(im) catalysts show similar iso-hexane selectivity. Both samples have much higher iso-hexane selectivity than the Ni/SAPO-11(im) which show a significant increase in cracking with n-hexane conversion (Fig. 10 (d)). In all cases, the iso-hexane selectivity follows the order: Ni/SAPO-11(s)  $\approx$  Pt/SAPO-11(im) > Ni/SAPO-11(im). The yield of iso-hexane over the Ni/SAPO-11(s) is slightly lower than that over the Pt/SAPO-11(im) at temperature below 613 K, while it exceeds the latter as the temperature increases continuously (Fig. 10 (b)). Most interestingly, the Ni/SAPO-11(s) and Pt/SAPO-11(im) catalysts have nearly the same maximum iso-hexane yield at ca. 66.7 % at 613 K. In contrast, the Ni/SAPO-11(im) has the lowest iso-hexane yield at all the

temperatures tested. Therefore, the Ni/SAPO-11(s) catalyst prepared by the novel direct synthesis method has comparable performance to the noble metalcatalyst Pt/SAPO-11(im) in terms of n-hexane conversion and iso-hexane selectivity. This resultsuggests that the Ni/SAPO-11(s) is a promising candidate for hydroisomerization catalysts.

A detailed products distribution for the Ni/SAPO-11(s), Ni/SAPO-11(im) and Pt/SAPO-11(im) at similar n-hexane conversion is shown in Table 2. The selectivity to iso-hexane over the Ni/SAPO-11(s), Ni/SAPO-11(im) and Pt/SAPO-11(im) is 95.1, 84.4 and 95.7%, respectively. The Ni/SAPO-11(s) catalyst and the Pt/SAPO-11(im) referencecatalyst exhibit similar selectivity to methyl pentanes (MP),92.8% and 94.6%, respectively. While the selectivity to methyl pentanes over Ni/SAPO-11(im) is only 81.3%. Ni/SAPO-11(s) and Ni/SAPO-11(im) show slightly higher selectivity to dimethyl butanes (DMB), 2.3 and 3.1%, respectively than that for the Pt/SAPO-11(im) (1.1%). This result indicates that nickel based hydroisomerization catalysts (Ni/SAPO-11(s) and Ni/SAPO-11(im)) favor the formation of di-branched isomers that have higher octane number than the mono-branched ones. It is consistent with the previous report by Eswaramoorthi and Lingappan, who found that the addition of nickel to Pt/H- $\beta$  or Pt/H-mordenite catalysts increased the n-hexane conversion and DMB selectivity, and they attributed this behavior to the metal-acid balance[60]. The Ni/SAPO-11(im) shows the highest selectivity to cracking products(15.6 %) vs the other catalysts Ni/SAPO-11(s)(4.9%) and Pt/SAPO-11(im) (4.3%). It might be attributed to the poor balance between (de)hydrogenation and acid functions which will be discussed later.

Table 2 Products distribution of n-hexane hydroisomerization over Ni/SAPO-11(s), Ni/SAPO-11(im) and Pt/SAPO-11(im) catalysts at the n-hexane conversion of 51.5 ( $\pm$ 2.0)%.

Sample	Ni/SAPO-11(s)	Ni/SAPO-11(im)	Pt/SAPO-11(im)
Conversion (%)	49.5	53.5	53.4
$S_I^a$ (%)	95.1	84.4	95.7
$S_{MP}^a$ (%)	92.8	81.3	94.6
2-MP	57.5	49.2	58.3
3-MP	35.3	32.1	36.3
$S_{DMB}^a$ (%)	2.3	3.1	1.1
2,2-DMB	0.1	0.5	-
2,3-DMB	2.2	2.6	1.1
$S_C^a$ (%)	4.9	15.6	4.3

<sup>a</sup> $S_{MP}$ ,  $S_{DMB}$ ,  $S_I$ , and  $S_C$  correspond to the selectivity to methyl pentanes, dimethyl butanes, iso-hexanes and cracking products, respectively.

High catalytic stability is also indispensable for practical application of the hydroisomerization catalyst. The stability of the Ni/SAPO-11(s) was studied preliminarily at 613 K and the result is shown in Fig. S6. The n-hexane conversion and iso-hexane yield exhibit a slight decrease during the initial 2 h and then remain almost constant. The iso-hexane selectivity experiences no significant change in spite of a slight increase in the initial 2 h. The results indicate that the Ni/SAPO-11(s) catalyst prepared via the novel method has a promising stability in the hydroisomerization of n-hexane.

### 3.7 Synergetic effect of metal and acid sites

The classical mechanism describing the alkanes hydroisomerization involves the following successive chemical steps: (i) dehydrogenation of alkanes into alkenes on metal sites, (ii) skeletal rearrangement of the alkenes on acid sites and (iii) hydrogenation of the branched alkenes to corresponding branched alkanes[32]. Thus, the catalytic behavior of the

hydroisomerization catalyst is closely related to features of (de)hydrogenation sites and acid sites as well as the balance between them. The Ni/SAPO-11(s) in comparison to the Ni/SAPO-11(im) exhibits enhanced activity, which is attributed to more accessible metal and acid sites. The Ni/SAPO-11(s) catalyst also demonstrates higher iso-hexane selectivity than the Ni/SAPO-11(im). The better metal-acid balance for the Ni/SAPO-11(s), which is confirmed by its higher  $C_{Ni}/C_A$  ratio (0.224) than that over the Ni/SAPO-11(im) (0.158, Table 1), is the first explanation for this phenomenon. Under such circumstance, each alkene intermediate comes into fewer acid sites during its diffusion from one Ni site to another[61]. Thus, the subsequent cracking reaction on acid sites is suppressed, resulting in high iso-hexane selectivity. In contrast, owing to the small amount of metal sites in the Ni/SAPO-11(im) catalyst, the alkene intermediates will confront acid sites that are relatively excessive and then crack into smaller molecules, thus reducing the iso-hexane selectivity. Another explanation could be the proximity between metal and acid sites. For an ideal isomerization catalyst, metal and acid sites should be close enough so that the number of acid sites between two metal sites is low enough to catalyze only one step of skeletal rearrangement[62]. It helps to reduce the probability of cracking the alkene intermediates during the diffusion from acid sites to the nearest metal sites. The Ni/SAPO-11(s) catalyst has better metal-acid balance and closer metal-acid proximity which is contributed by the small metal particles. It seems to have higher level of ideality in terms of synergetic effect between metal and acid sites, which can be evidenced by the reaction pathway and products distribution as discussed later.

The cracking/isomer (C/I) and di-branched/mono-branched (DMB/MP) ratios vs. n-hexane

conversions over the Ni/SAPO-11(s), Ni/SAPO-11(im) and Pt/SAPO-11(im) catalysts are shown in Fig. 11. When the n-hexane conversion is extrapolated to zero, the high DMB/MP value over the Ni/SAPO-11(im) indicates that both the di-branched and mono-branched isomers are primary products. The DMB/MP and C/I ratios increase significantly with n-hexane conversion, indicating the large number of transformation of mono-branched isomers to di-branched or even cracking products. It seems that the n-hexane hydroisomerization over the Ni/SAPO-11(im) follows the route shown in Fig. 12 (a), which is attributed to the poor metal-acid balance. However, for Ni/SAPO-11(s) or Pt/SAPO-11(im), the DMB/MP and C/I ratios are approximately zero when the n-hexane conversion is extrapolated to zero, and they increase slightly until the n-hexane conversion reaches 70.0 %. This implies that n-hexane hydroisomerization over the Ni/SAPO-11(s) follows a successive route (Fig. 12 (b)). Through this route, the alkene intermediates prefer to be hydrogenated on the metal sites, instead of further transformed on acid sites, which is evidenced by the predominant content of mono-branched isomers in the isomer products (Fig. S7). Therefore, the catalytic behavior of the Ni/SAPO-11(s) is superior to the Ni/SAPO-11(im) prepared by impregnation.

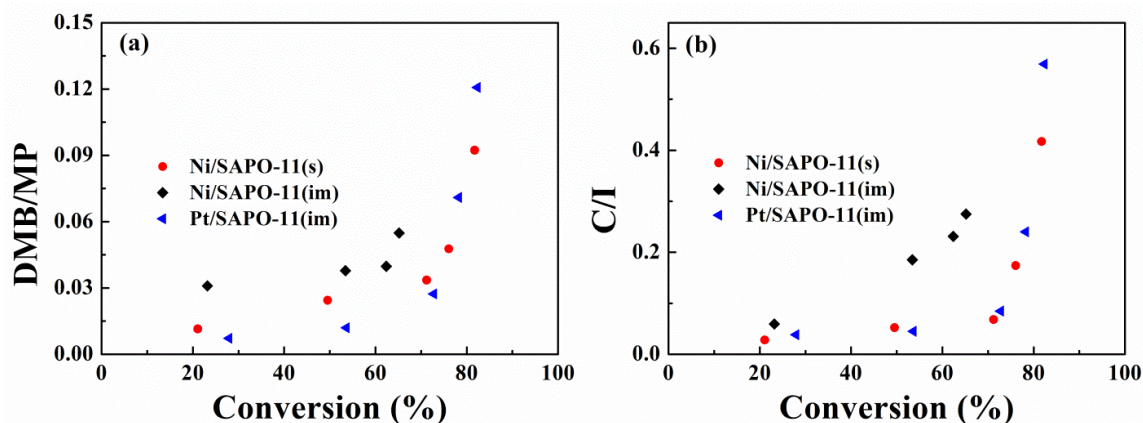


Fig.11. The product distribution of n-hexane hydroisomerization over Ni/SAPO-11(s), Ni/SAPO-11(im)

and Pt/SAPO-11(im) catalysts: (a) di-branched/mono-branched and (b) cracking/isomer ratios vs. n-C<sub>6</sub> conversions

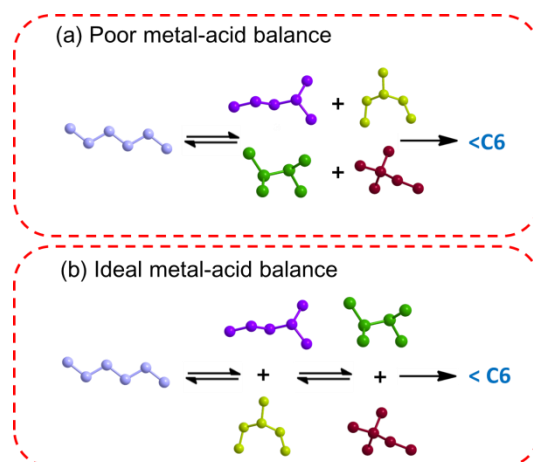


Fig. 12. Reaction pathways of n-hexane hydroisomerization over catalysts with (a) poor and (b) ideal metal-acid balance

The skeletal rearrangements of alkene intermediates on the acid sites are suggested to be the rate limiting step over the Ni/SAPO-11(s), according to the reaction pathway and products distribution. In order to verify this point, different ratios of metal sites to acid sites ( $C_{Ni}/C_A$ ) were attained in the Ni/SAPO-11(s) catalysts by varying nickel loading. The n-hexane conversion and turn over frequency ( $TOF_{n-C_6}$ ) per acid site as a function of  $C_{Ni}/C_A$  are shown in Fig. S8. They increase at  $C_{Ni}/C_A < 0.193$ , and then remain constant at higher  $C_{Ni}/C_A$  values. Similar phenomenon has been observed for noble metal based bifunctional catalyst.[62] This result is in agreement with the change in rate limiting reaction: from (de)hydrogenation on the nickel sites at low  $C_{Ni}/C_A$  values, to skeletal arrangements on the acid sites at high values. Therefore, the hypothesis proposed earlier is confirmed by the results presented for the Ni/SAPO-11(s) catalyst with a  $C_{Ni}/C_A$  of 0.224.

The insufficient acid sites limit the hydroisomerization process over Ni/SAPO-11(s), and therefore H-Beta zeolite was added in the synthesis system of Ni/SAPO-11(s) to increase the

acidity and improve the catalytic performance. The final crystalline product was named as Ni/SAPO-11- $\beta$ (s). The total acid sites increase to 374.1  $\mu\text{mol/g}$  for sample Ni/SAPO-11- $\beta$ (s). The number of accessible metal sites over the Ni/SAPO-11- $\beta$ (s) (54.6  $\mu\text{mol/g}$ ) is similar to that over the Ni/SAPO-11(s). The catalytic performance of the Ni/SAPO-11- $\beta$ (s) catalyst at 613 K is shown in Fig. 13. The n-hexane conversion and iso-hexane yield over the Ni/SAPO-11(s) are 71.2% and 66.7%, respectively while they increase to 80.9% and 73.3% over the Ni/SAPO-11- $\beta$ (s), respectively. The n-hexane conversion and iso-hexane yield are also higher than the corresponding values over the classical catalyst Pt/SAPO-11(im) (72.8% and 67.1%). Besides, the Ni/SAPO-11- $\beta$ (s) has approximately 9 and 10 times higher selectivity to di-branched isomers compared to catalysts Ni/SAPO-11(s) and Pt/SAPO-11(im), respectively. Most interestingly, with reducing the reaction temperature to 593 K, no significant change in the n-hexane conversion (79.3%) is observed. While the yield of iso-hexane increases to 76.0%, which is among the highest values reported for n-hexane hydroisomerization to our knowledge up to now. Therefore, the nickel based catalyst prepared via the direct synthesis method shows promising catalytic properties.

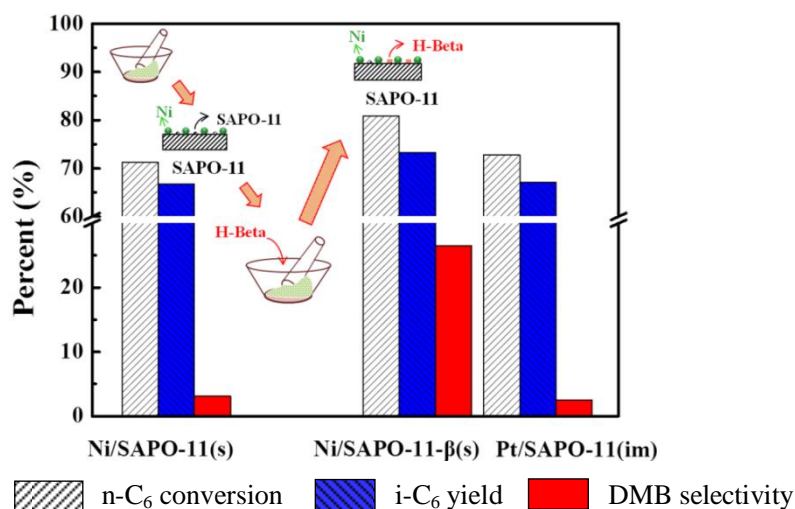


Fig.13. Catalytic performance of the Ni/SAPO-11(s), Ni/SAPO-11- $\beta$ (s) and Pt/SAPO-11(im) samples at

613 K, 2.0 MPa,  $H_2/n-C_6 = 4.0$  and  $WHSV = 1.0 h^{-1}$

## 4. Conclusions

The Ni/SAPO-11(s) hydroisomerization catalyst with high dispersion of nickel species was prepared via the novel direct synthesis method; the nickel species and acid sites were instantaneously formed in the catalyst. Three types of nickel species in the catalyst were identified. The metallic nickel is the main active site for (de)hydrogenation and framework nickel supplies more acid sites for the n-hexane hydroisomerization. A great balance between the metal and the acid sites was achieved via the direct synthesis method. The isomerization of alkene intermediates on the acid sites is the rate limiting step. The Ni/SAPO-11(s) catalyst exhibits one of the highest iso-hexane yields reported in the hydroisomerization of n-hexane. The novel direct synthesis method opens a new door for preparation of metal supported catalysts.

## Acknowledgements

This work was supported by the “Fundamental Research Funds for the Central Universities (Grant No. 16CX06012A)”, the “Shandong Province Natural Science Foundation of China” (Grant No. 2013ZRE28069), and the “National Natural Science Foundation of China” (Grant No. 21376267).

## References

- [1] J. Pastvova, D. Kaucky, J. Moravkova, J. Rathousky, S. Sklenak, M. Vorokhta, L. Brabec, R. Pilar, I. Jakubec, E. Tabor, P. Klein, P. Sazama, *ACS Catal.* (2017) 5781-5795.
- [2] K. An, S. Alayoglu, N. Musselwhite, K. Na, G.A. Somorjai, *J. Am. Chem. Soc.* 136 (2014) 6830-6833.

- [3] V.M. Akhmedov, S.H. Al-Khowaiter, *Catal. Rev.* 49 (2007) 33-139.
- [4] N.V. Chekantsev, M.S. Gyngazova, E.D. Ivanchina, *Chem. Eng. J.* 238 (2014) 120-128.
- [5] H. Song, L. Zhao, N. Wang, F. Li, *Appl. Catal. A: Gen.* 526 (2016) 37-44.
- [6] N.A.A. Fatah, S. Triwahyono, A.A. Jalil, A. Ahmad, T.A.T. Abdullah, *Appl. Catal. A: Gen.* 516 (2016) 135-143.
- [7] G. Ye, Y. Sun, Z. Guo, K. Zhu, H. Liu, X. Zhou, M.-O. Coppens, *J. Catal.* 360 (2018) 152-159.
- [8] C.-H. Geng, F. Zhang, Z.-X. Gao, L.-F. Zhao, J.-L. Zhou, *Catal. Today* 93-95 (2004) 485-491.
- [9] S. Parmar, K.K. Pant, M. John, K. Kumar, S.M. Pai, B.L. Newalkar, *J. Mol. Catal. A: Chem.* 404-405 (2015) 47-56.
- [10] Y. Wang, Z. Tao, B. Wu, J. Xu, C. Huo, K. Li, H. Chen, Y. Yang, Y. Li, *J. Catal.* 322 (2015) 1-13.
- [11] P. Wang, J. Zhang, G. Wang, C. Li, C. Yang, *J. Catal.* 338 (2016) 124-134.
- [12] C. Erkey, *J. Supercrit. Fluids* 47 (2009) 517-522.
- [13] Y. Lyu, Y. Liu, L. Xu, X. Zhao, Z. Liu, X. Liu, Z. Yan, *Appl. Surf. Sci.* 401 (2017) 57-64.
- [14] S.-S. Liu, Y.-Y. Jin, Y. Han, J. Zhao, J. Ren, *Fuel Process. Technol.* 177 (2018) 266-274.
- [15] S. Wang, Y. Wang, C. Hu, *Int. J. Hydrogen Energy* 43 (2018) 13921-13930.
- [16] S.-W. Ho, Y.-S. Su, *J. Catal.* 168 (1997) 51-59.
- [17] M.F. Variava, T.L. Church, N. Noorbehesht, A.T. Harris, A.I. Minett, *Catal. Sci. Technol.* 5 (2015) 515-524.
- [18] M. Tao, X. Meng, Y. Lv, Z. Bian, Z. Xin, *Fuel* 165 (2016) 289-297.

- [19] F.T. Zangeneh, S. Mehrazma, S. Sahebdehfar, *Fuel Process. Technol.* 109 (2013) 118-123.
- [20] C. Papadopoulou, J. Vakros, H.K. Matralis, C. Kordulis, A. Lycourghiotis, *J. Colloid Interf. Sci.* 261 (2003) 146-153.
- [21] M.A. Goula, N.D. Charisiou, K.N. Papageridis, A. Delimitis, E. Pachatouridou, E.F. Iliopoulou, *Int. J. Hydrogen Energy* 40 (2015) 9183-9200.
- [22] J.L. Ewbank, L. Kovarik, F.Z. Diallo, C. Sievers, *Appl. Catal. A: Gen.* 494 (2015) 57-67.
- [23] G. Wang, H. Wang, H. Zhang, Q. Zhu, C. Li, H. Shan, *ChemCatChem* 8 (2016) 3137-3145.
- [24] J. Wu, Z. Peng, A.T. Bell, *J. Catal.* 311 (2014) 161-168.
- [25] S. Wang, G.Q. Lu, *Appl. Catal. B: Environ.* 19 (1998) 267-277.
- [26] K. Fang, J. Ren, Y. Sun, *J. Mol. Catal. A: Chem.* 229 (2005) 51-58.
- [27] R.B. Duarte, O.V. Safonova, F. Krumeich, J.A. van Bokhoven, *Phys. Chem. Chemical Phys.* 16 (2014) 26553-26560.
- [28] Y. Jin, Q. Sun, G. Qi, C. Yang, J. Xu, F. Chen, X. Meng, F. Deng, F.-S. Xiao, *Angew. Chem.* 125 (2013) 9342-9345.
- [29] Y. Du, B. Feng, Y. Jiang, L. Yuan, K. Huang, J. Li, *Eur. J. Inorg. Chem.* 2018 (2018) 2599-2606.
- [30] G.E. Giannetto, G.R. Perot, M.R. Guisnet, *Ind. Eng. Chem. Prod. Res. Develop.* 25 (1986) 481-490.
- [31] F. Alvarez, F.R. Ribeiro, G. Perot, C. Thomazeau, M. Guisnet, *J. Catal.* 162 (1996) 179-189.

- [32] J.E. Samad, J. Blanchard, C. Sayag, C. Louis, J.R. Regalbuto, *J. Catal.* 342 (2016) 203-212.
- [33] S. Zhang, S.-L. Chen, P. Dong, G. Yuan, K. Xu, *Appl. Catal. A: Gen.* 332 (2007) 46-55.
- [34] M.Y. Kim, K. Lee, M. Choi, *J. Catal.* 319 (2014) 232-238.
- [35] R. Garcia, I.J. Shannon, A.M.Z. Slawin, W. Zhou, P.A. Cox, P.A. Wright, *Micropor. Mesopor. Mat.* 58 (2003) 91-104.
- [36] Y.-H. Xu, Z. Yu, X.-F. Chen, S.-H. Liu, X.-Z. You, *J. Solid State Chem.* 146 (1999) 157-162.
- [37] Y. Meng, H.C. Genuino, C.-H. Kuo, H. Huang, S.-Y. Chen, L. Zhang, A. Rossi, S.L. Suib, *J. Am. Chem. Soc.* 135 (2013) 8594-8605.
- [38] G. Garbarino, S. Campodonico, A.R. Perez, M.M. Carnasciali, P. Riani, E. Finocchio, G. Busca, *Appl. Catal. A: General* 452 (2013) 163-173.
- [39] Y. Zhao, B. Liu, R. Amin, *Ind. Eng. Chem. Res.* 55 (2016) 6931-6942.
- [40] X. Gao, H. Mao, M. Lu, J. Yang, B. Li, *Micropor. Mesopor. Mat.* 148 (2012) 25-33.
- [41] M.H.M. Ahmed, O. Muraza, A.K. Jamil, E.N. Shafei, Z.H. Yamani, K.-H. Choi, *Energy Fuels* 31 (2017) 5482-5490.
- [42] E. Heracleous, A.F. Lee, K. Wilson, A.A. Lemonidou, *J. Catal.* 231 (2005) 159-171.
- [43] C. Ragupathi, J.J. Vijaya, P. Surendhar, L.J. Kennedy, *Polyhedron* 72 (2014) 1-7.
- [44] M.A. Peck, M.A. Langell, *Chem. Mater.* 24 (2012) 4483-4490.
- [45] R.J.O. Mossanek, I. Preda, M. Abbate, J. Rubio-Zuazo, G.R. Castro, A. Vollmer, A. Gutiérrez, L. Soriano, *Chem. Phys. Lett.* 501 (2011) 437-441.
- [46] A. Śrębowata, R. Baran, D. Łomot, D. Lisovyt'skiy, T. Onfroy, S. Dzwigaj, *Appl. Catal.*

- B: Environ. 147 (2014) 208-220.
- [47] L. Zhao, Y. Wang, H. An, X. Zhao, Y. Wang, Catal. Commun. 103 (2018) 74-77.
- [48] A.N. Kharat, P. Pendleton, A. Badalyan, M. Abedini, M.M. Amini, J. Catal. 205 (2002) 7-15.
- [49] A. Dugué, O. Dymshits, L. Cormier, B. Cochain, G. Lelong, S. Belin, A. Zhilin, J. Non-Crystal. Solids 413 (2015) 24-33.
- [50] P. Lin, Y. Fu, Spectrosc. Lett. 34 (2001) 83-92.
- [51] S.D. Kelly, N. Yang, G.E. Mickelson, N. Greenlay, E. Karapetrova, W. Sinkler, S.R. Bare, J. Catal. 263 (2009) 16-33.
- [52] Y. Li, B. Zhang, X. Xie, J. Liu, Y. Xu, W. Shen, J. Catal. 238 (2006) 412-424.
- [53] S. Das, S. Thakur, A. Bag, M.S. Gupta, P. Mondal, A. Bordoloi, J. Catal. 330 (2015) 46-60.
- [54] A. Masalska, Appl. Catal. A: Gen. 294 (2005) 260-272.
- [55] S. Tian, J. Chen, Fuel Process. Technol. 122 (2014) 120-128.
- [56] L. Guo, Y. Fan, X. Bao, G. Shi, H. Liu, J. Catal. 301 (2013) 162-173.
- [57] S. Inagaki, K. Sato, S. Hayashi, J. Tatami, Y. Kubota, T. Wakihara, ACS Appl. Mat. Interf. 7 (2015) 4488-4493.
- [58] D. Arias, I. Campos, D. Escalante, J. Goldwasser, C.M. López, F.J. Machado, B. Méndez, D. Moronta, M. Pinto, V. Sazo, M.M.R. de Agudelo, J. Mol. Catal. A: Chem. 122 (1997) 175-186.
- [59] X. Yang, H. Ma, Z. Xu, Y. Xu, Z. Tian, L. Lin, Catal. Commun. 8 (2007) 1232-1238.
- [60] I. Eswaramoorthi, N. Lingappan, Korean J. Chem. Eng. 20 (2003) 207-216.

[61] M. Guisnet, *Catal. Today* 218-219 (2013) 123-134.

[62] N. Batalha, L. Pinard, C. Bouchy, E. Guillon, M. Guisnet, *J. Catal.* 307 (2013) 122-131.